The 8th International Conference on Jets, Wakes and Separated Flows, ICJWSF-2024
September 23-25, 2024, Firenze, Italy

Effect of different tessellation modifications of bluff bodies on boundary layer transition

N. Beratlis[1], K. Squires[1] and E. Balaras[2*]

1: School for Engineering of Matter, Transport and Energy, Arizona State University, USA
2: Department of Mechanical and Aerospace Engineering, The George Washington University, USA

[*] Corresponding author: balaras@gwu.edu

Abstract

In this study, the effect of different tessellations on the transition to supercritical flow and the subsequent evolution of the boundary layers is investigated. The drag on tessellated spheres, comprising mostly hexagonal flat panels, for a wide range of Reynolds number is measured by wind tunnel experiments. Direct numerical simulations (DNS) are also carried out to provide and in depth analysis on the boundary layer evolution and explain the differences on the drag coefficient. The skin friction, pressure, velocity profiles and the turbulent kinetic energy are used to identify the location of the transition point and explain the differences in the evolution of the boundary layer. Agreement between the DNS and the experimental measurements is very good.

Keywords: *Tessellation, Drag reduction, Transition*

1. Introduction

Various passive roughness elements, have been used in the past to trip the boundary layer over bluff bodies. Among the most popular methods are wires, dimples and sand-grain roughness, with each having distinct impact on the transition process and the evolution of the boundary layer. For instance, Choi *et al.* [9] carried out wind tunnel tests to study the effect of trip wires on spheres. They used a multi-channel hot-wire anemometer and a single hot-wire probe to measure the boundary layer velocity profiles. They concluded that as the boundary layer encounters the trip wire, the flow separates locally creating a shear layer. At high Reynolds number the shear layer becomes unstable and introduces disturbances to the boundary layer which becomes fully turbulent and delays the main separation. For sand grain roughness, Achenbach [1] showed that using small glass beads or sand paper to roughen the surface of the sphere the drag crisis can be significantly accelerated. As the size of the roughness elements increases the critical Reynolds number is reduced. However the minimum drag coefficient can not be maintained and rises very quickly as the Reynolds number is increased. Finally, dimples are another form of roughness elements commonly employed to trip the boundary layer. A number of investigators carried out wind tunnel experiments on dimpled spheres (see [8], [5], [3], [2]). The majority of the experiments consisted of mounting prototypes in the wind tunnel and measuring the drag as function of the Reynolds number. Overall this body of work indicates that the dimple topology has an impact on the critical Reynolds number, as well as the minimum attained drag coefficient. In general as the dimple volume is increased the drag crisis is accelerated and the drag coefficient in the post-critical regime increases. Choi *et al.* [8] used surface oil flow visualization to identify the global separation line and measured the streamwise velocity inside and around the dimples. In particular, they found that dimples cause local flow separation leading to the formation of a detached shear layer that becomes unstable resulting in the generation of turbulence, which causes transport of high speed fluid closer to the wall. They also showed that as the Reynolds number is increased the transition point moves gradually upstream but the global separation point remains unchanged.

Recently Beratlis *et al.* [6] presented a novel topological modification, comprising of the tessellation of a sphere, resulting in spherical polyhedral containing mostly hexagonal and some pentagonal flat panels. They carried out both wind tunnels tests and measured the drag on tessellated spheres for a range of Reynolds numbers. The measurements showed that the variation of the drag coefficient as a function of the Reynolds number for a tessellated sphere is very similar to that of a dimpled sphere: drag crisis occurs and the drag coefficient remains relatively constant in the post-critical regime. However tessellated spheres exhibited 10%-15% lower drag in the post-critical regime compared to dimples without a change in the critical Reynolds number. To investigate the source of drag reduction the authors carried out direct numerical simulations of both a tessellated and a dimple sphere at the same Reynolds number. The analysis showed the tessellated spheres exhibit a slightly smaller pressure penalty on the front part and more importantly separation is delayed by 10° compared to a dimpled sphere at the same Reynolds number, which accounts for the majority of the drag reduction. In this work we will study the effect of different tessellations on the transition process and the evolution of the boundary layers. The drag on tessellated spheres for a wide range of Reynolds number is measured by wind tunnel experiments. Direct numerical simulations are also carried out to provide and in depth analysis on the boundary layer evolution and explain the difference behavior of the drag curve. A summary of the methods will be given next followed by results and conclusions.

2. Methodologies

Both wind tunnel experiments and direct numerical simulations have been carried out. The experiments have been carried out in an open return wind tunnel at the George Washington University with a test section of $30cm \times 25cm \times 70cm$ in the spanwise, vertical and streamwise direction respectively running at speeds between $18 - 63\ m/s$. The drag on various spheres was measured using a single component piezoelectric force sensor mounted on a sting on one end and attached to the back of the spheres on the other end. The sensor had a diameter of $0.6cm$ and width of $0.2cm$. The sting itself was attached to a rigid test stand located approximately $20cm$ behind the spheres. A very thin piano wire $0.05cm$ in diameter was wrapped around the sting and securely attached to the floor of the test section to reduce the vibrations on the spheres. The sphere models had a diameter of $6.85cm$ and were fabricated via 3D printing using a *Projet 3500* machine. In particular, two tessellated sphere were considered, one with 162 panels, consisting of 150 hexagonal and 12 pentagonal flat faces, and one with 192 panels, consisting of 180 hexagonal and 12 pentagonal flat faces. The blockage ratio was 4.7% which is below the generally accepted 5% threshold [4]. For validation the drag coefficient of a smooth sphere in the sub-critical regime ($8.0 \times 10^{4} < Re < 2.2 \times 10^{5}$) was measured, and was in agreement to prior experiments in the literature.

For the numerical simulations the Navier-Stokes equations for viscous incompressible flow are solved on a structured grid in cylindrical coordinates. In the following the letters r, ϕ, and z denote the radial, azimuthal and axial coordinates respectively, while θ denotes the polar angle, going from $\theta = 0^{\circ}$ at the stagnation point at the front of the sphere to $\theta = 180^{\circ}$ at wake side. The immersed boundary formulation proposed by Yang and Balaras [11] is utilized to imposed boundary conditions on the surface of the sphere. The computational domain extends $10D$ upstream and $30D$ downstream of the sphere (the center of the sphere is located at $r/D = 0$, $z/D = 0$, where r and z are the radial and axial coordinates respectively). The computational grid consists of $1100 \times 3002 \times 3002$ points in the radial, azimuthal and axial directions respectively. The grid resolution is very similar to the one used in DNS of the flow over a dimpled sphere [7], which is sufficient to resolve the dominant flow structures near the wall as well as in the near wake. In particular, near the top of the sphere ($\theta = 90^{\circ}$) where the skin friction reaches its maximum value, the grid resolution in the wall normal direction $\Delta r^{+} \sim 1.0$, while $\Delta \phi^{+} \sim 10.0$ and $\Delta z^{+} \sim 8.0$. The Reynolds number, based on the freestream velocity U, sphere diameter D and the kinematic viscosity ν, was set to $Re = 1.5 \times 10^{5}$.

3. Discussion

Fig. 1 shows the variation of the drag coefficient with Reynolds number measured in the wind tunnel for one dimpled sphere and for two polyhedral spheres, one with 162 and 192 polygonal panels (referred to from now on as poly162 and poly192 respectively). The ratio of frontal area to that of a smooth sphere is also very close to 1, with the poly192 and poly162 being 0.986 and 0.982 respectively. Therefore the reduction in the drag coefficient exhibited by the above polyhedral and shown next can not be attributed to changes in the frontal area. The drag curves for the polyhedral and dimpled spheres are very similar, with the polyhedral exhibiting a drag crisis around $Re \sim 8 \times 10^{4}$ and maintaining the low drag in the post-critical regime. In general, as the number of polygonal panels increases, the polyhedral approaches a smooth sphere and the

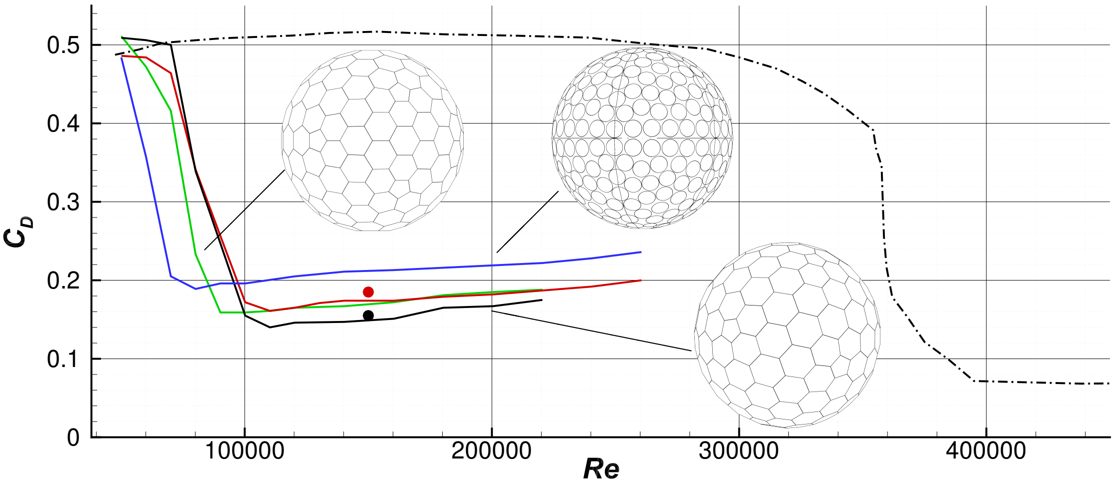

Fig. 1: Drag coefficient vs Reynolds number for various spheres. —·— smooth sphere [1]; —— dimpled sphere with dimple depth $k = 0.0035D$ (present experiment); —— dimpled sphere with $k = 0.003D$ (present experiment); —— icosahedral sphere with 192 polygonal panels (present experiment); —— icosahedral with 162 polygonal panels (present experiment); • icosahedral with 192 polygonal panels (present DNS); • icosahedral with 162 polygonal panels (present DNS); • dimpled sphere with $k = 0.003D$ (present DNS).

drag crisis shifts towards higher Reynolds numbers while the drag coefficient in the post-critical regime decreases. The predicted drag coefficient from the present DNS is shown with solid circles. The agreement with the experimental results is very good with the DNS values are within 2-3% of the experiments. The drag coefficient, $C_D = D/(0.5\rho U^2 A)$, in the post-critical regime for poly162 and poly192 is 0.178 and 0.155 respectively.

To better understand the trends in Fig. 1 we will compare the results from the corresponding DNS. Fig. 2 shows contours of the time-averaged skin friction coefficient, $\overline{C}_f = 2\nu/U^2 \times d\overline{U}_t/dn$, ($\overline{U}_t$ is the time averaged tangential velocity minus the azimuthal component and n is the surface normal), for the two polyhedrals. The separation line is indicated by a black line and the polar angle θ measured from the stagnation point at the front is denoted by vertical dashed lines. For the poly162 the flow separates locally over the leading edge of a flat panel as early as 76°. The exact location of the flat panel is indicated by a thick black arrow and its perimeter is highlighted with a thin grey line. The separation bubble is small and the flow reattaches before the middle of the panel. Small local separation bubbles are again observed at 80° and they appear to be present more consistently over multiple panels in the azimuthal direction. For poly192 the behavior of the skin friction is similar but the first local separation bubbles start occurring a little later, around $\theta = 80^\circ$ and more consistently in the azimuthal direction closer to $\theta = 90^\circ$.

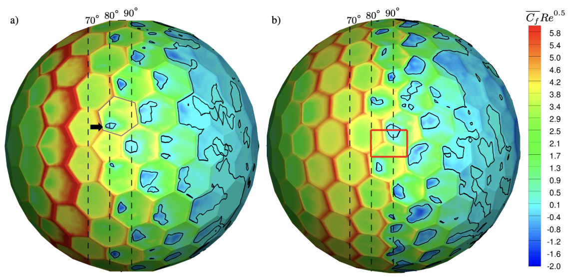

Fig. 2: Contours of the time-average skin friction coefficient, $\overline{C}_f$, scaled by $Re^{0.5}$. a) poly162; b) poly192. The separation line is shown with a solid black line while the polar angle at various locations is indicated by vertical dashed lines. The red rectangular outline corresponds to the location of the hexagonal dimple shown in Fig. 4.

Fig. 3a shows the skin friction coefficient, $\overline{C}_f$, averaged over time and the azimuthal direction. The average surface depth distribution k/D is also plotted at the bottom. The depth is measured relative to the surface of a smooth sphere of diameter D. For the case of the poly162 k/D exhibits considerable variation while for poly192 it is more uniform and also consistently lower. Overall, $\overline{C}_f$ at the front part of the polyhedral exhibits local peaks and valleys consistent with those of the depth k/D. The maximum in C_f is observed at $\theta = 60^{\circ}$ and it is higher for poly162. Global separation, identified as the cross from positive to negative values of C_f, occurs at $\theta = 120^{\circ}$ and $\theta = 126^{\circ}$ for the poly162 and poly192 respectively. The integral of the skin friction as a function of θ is shown in Fig. 3b. When the integral is evaluated over the entire sphere it is equal to the skin friction drag. In the front part of both polyhedral ($\theta < 45^{\circ}$) the integral of the skin friction is very similar. For $\theta > 45^{\circ}$ the skin friction drag for poly162 is slightly larger than that of poly192. This is consistent with the higher maximum value of C_f observed for poly192. Overall the skin friction drag for both polyhedral is less than 10% of the total drag.

The distribution of the average pressure coefficient, $\overline{C_p}$, together with the average surface depth, k/D, as a function of θ is shown in Fig. 3c. For poly192, $\overline{C_p}$ is relatively smooth while for poly162 it exhibits small oscillations that are correlated with the average depth k/D. At the back of the sphere ($90^{\circ} < \theta < 125^{\circ}$) $\overline{C_p}$ for poly192 is lower. However due to the delayed separation it recovers to a greater value and remains consistently higher than that of poly162. As for $\overline{C_f}$ above, the integral of C_p as a function of θ is shown in Fig. 3d. For $0^{\circ} < \theta < 45^{\circ}$ the pressure integrals are very close. For $\theta > 55^{\circ}$ poly162 start to incur a small pressure penalty relative to the poly192. Approximately 50% contribution to the additional drag for poly162 comes form the lower back pressure due to the earlier separation. The difference in the separation point between the two types of spheres can be explained by looking at the evolution of the boundary layer. First of all, the approximate location of transition to turbulence can be determined by looking at the behavior of the velocity fluctuations. The turbulent kinetic energy, $\overline{q}$, averaged over time and in the azimuthal direction (not shown here) is negligible at the front part for both polyhedral and they start to rise around $\theta = 82^{\circ}$ and $\theta = 87^{\circ}$ for poly162 and poly192 respectively. It is therefore reasonable to assume that transition to turbulence occurs a little earlier for the poly162. The location of the peak (around $\theta = 115^{\circ}$) and the maxima values in q are very similar between the two cases.

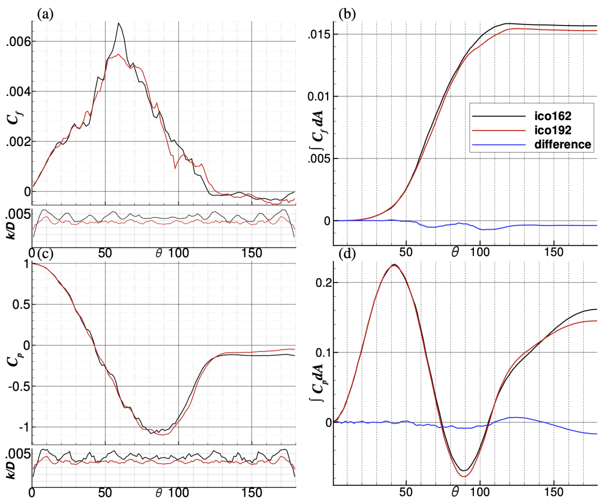

Fig. 3: a) Distribution of the average skin friction coefficient, C_f, (top part) and average surface depth (bottom part); b) Integral of C_f. c) Distribution of the average pressure coefficient C_p (top part) and average surface depth (bottom part); d) Integral of C_p. –; poly162, –; poly192; ——— difference between poly192 and poly162.

Fig. 4 shows contours of the instantaneous azimuthal vorticity at a plane cutting through the middle of one of the hexagonal flat panels near the top of poly192 sphere where transition occurs. Contours of the instantaneous skin friction coefficient, C_f, are plotted on the surface of the sphere along with the separation line denoted by a black line. It is clearly seen that a shear layer is formed as the flow separates over the leading edge of the flat hexagonal panel. The flow separation is not uniform across the span and occurs over a small portion near the first half of the panel. The flow reattaches again near the center of the panel. Shortly after the flow separates the shear layer becomes unstable and starts to roll-up into vortical structures, annotated as rollers A and B in the figure. The evolution of these rollers, which is essential in the transition process, can be better traced in Fig. 4b, where a top view is shown and the vortical structures are colored by their streamwise vorticity. It can be seen that roller A is not uniform in the azimuthal direction and does not extend across the entire span of panel. A similar behaviour can be observed for roller B. As these rollers undergo instabilities in the azimuthal direction their vorticity is reoriented from the azimuthal to the streamwise direction. Also, in between the two rollers pairs of counter-rotating streamwise vortices are present. These vortices are reminiscent of the braid-vortices containing mainly streamwise vorticity of opposite sign, typically found in free-shear layers undergoing Kevin-Helmhotz type instability. Towards the end sides of the rollers thin elongated vortices aligned in the sreamwise direction and containing streamwise vorticity are observed. Farther downstream and close to the trailing edge of the dimple various vortical

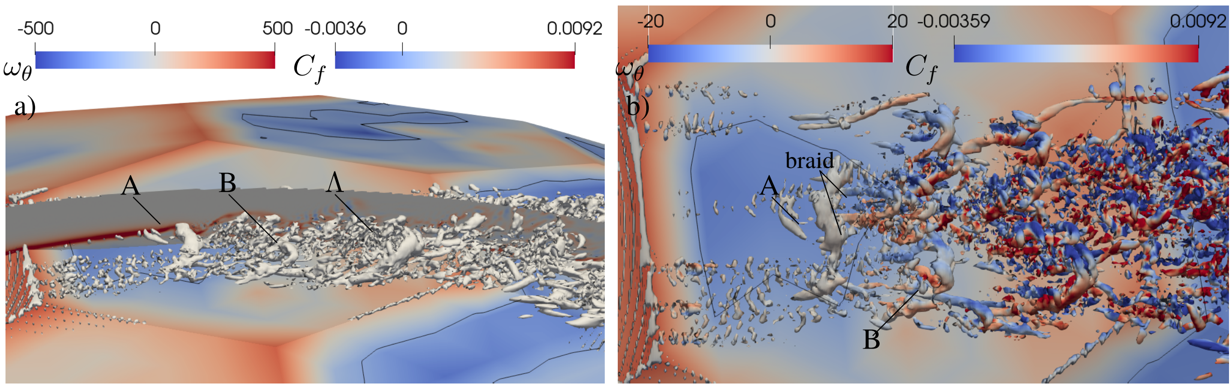

Fig. 4: a) Isosurface of the *Q-criterion* visualizing vortical structures near the top of the tesselated sphere. Contours of the instantaneous azimuthal vorticity, ω_θ, are also shown at an azimuthal plane going through the middle of a hexagonal panel along with contours of the instantaneous skin friction, C_f, plotted on the surface of poly192. The separation line is denoted by solid black line. The location of the hexagonal panel is indicated with a red box in Fig. 2b. b) Top view with vortical structures colored by contours of tangential vorticity ω_t.

structures resembling a Λ-type vortex are clearly observed. This pack of Λ-type vortices has evolved from the continuous bending of a previously shed roller and its legs are connected to a pair of braid vortices. We should note that the rollers aligned primarily in the azimuthal direction are transformed into Λ-type vortices always within the length of one panel for a given Reynolds number. This mechanism is qualitatively similar to the one observed for flow over a dimpled sphere [7].

Fig. 5 shows the average boundary layer thickness, δ, as a function of the polar angle θ, up to the separation point. Since the location of the wall varies in the azimuthal direction the boundary layer thickness is first calculated at each azimuthal plane, as shown in the insert of Fig. 5. This gives a set of displacement thicknesses δ_1 , δ_2, ... , δ_{n_ϕ} with respect to the local wall location, which are then averaged over the azimuthal direction ϕ to give $\overline{\delta}$. Note that $\overline{\delta}$ is calculated utilizing the vorticity definition proposed by [10], which is more appropriate in the presence of curvature and pressure gradients. The boudnary layer doesn't grow in a linear fashion. At the front part of the polyhedral and up to $\theta = 50^\circ$ the boundary layer grows very slowly. From $\theta = 50^\circ$ 80° the growth is faster and after 80° as the boundary layer becomes turbulent the growth ramps up significantly. For poly162 the rapid turbulent boundary layer growth occurs around 82° while for poly192 it occurs a little later, around $\theta = 87^\circ$. After that the rate of boundary layer growth is similar, but the boundary layer for poly162 remains consistently thicker than that of poly192. As a result of the thicker boundary global separation occurs earlier for the former.

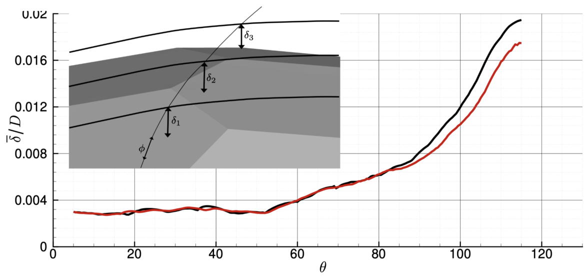

Fig. 5: Plot of the boundary layer thickness $\overline{\delta}$ averaged over time and azimuthal direction. Lines represent: –; poly162, –; poly192.

4. Conclusions

We report wind tunnel measurements of the drag coefficient over a range of Reynolds numbers, as well as DNS on spheres with a novel method of generating surface roughness. The method involves the process of tessellation by which the surface of a bluff body is approximated by plurality of predominantly hexagonal flat panels. Two spheres with 162 and 192 polygonal panels are considered. The wind tunnel measurements demonstrate that the variation of the drag coefficient as a function of the Reynolds number for the two tessellated spheres exhibits the typical behavior as a sphere albeit at a much lower critical Reynolds number: drag crisis occurs and the drag coefficient remains relatively constant in the post-critical regime. As the number of tessellations increases the drag crisis shifts towards higher Reynolds number and the value of the drag coefficient in the post-critical regime is reduced. However, compared to other commonly employed surface modifications that also exhibit similar behavior, namely dimples, the tessellation appears to be more efficient because the post-critical drag coefficient can be further reduced without affecting the critical Reynolds number where the drag crisis happens, or the drag crisis can be accelerated without incurring a drag penalty.

Detailed analysis of the results from the numerical simulations showed that tessellation induces transition to turbulence through a shear layer instability as the flow locally separates at the leading edge of the hexagonal panels. The location of the separation is tracked by observing the footprint of the time-averaged skin friction on the surface of the spheres. It is found that as the number of tessellated panels is reduced the local separation bubbles move upstream and closer to the stagnation point. The transition point which is identified by plotting the evolution of the turbulent kinetic energy close to the wall exhibits the same trend. Following transition it is observed that the boundary layer grows thicker at a faster rate. As a result, the tessellated sphere with the smaller number of panels starts growing thicker earlier, has less momentum near the wall and the flow separates earlier. Comparison of the average skin friction on the surface of the spheres reveals that global flow separation occurs at $\theta = 120^\circ$ and $\theta = 126^\circ$ for poly162 and poly192 respectively. The delayed separation for the latter helps the back pressure recover to a higher value, which in turns accounts for a lower form-drag.

References

[1] E. Achenbach. "Experiments on the flow past spheres at very high Reynolds numbers". In: *Journal of Fluid Mechanics* 54.3 (1972), pp. 565–575.

[2] K. Aoki, K. Muto, and H. Okanaga. "Mechanism of Drag Reduction by Dimple Structures on a Sphere". In: *Journal of Fluid Science and Technology* 7.1 (2012), pp. 1–10.

[3] K. Aoki et al. "Aerodynamic characteristic and flow pattern on dimples structure of a sphere". In: *10th International Conference on Fluid Control, Measurements, and Visualization* (2009). Moscow, Russia.

[4] H.B Awbi and S. Tan. "Effect of Wind-Tunnel Walls on the Drag of a Sphere". In: *Journal of Fluids Engineering-transactions of The Asme - J FLUID ENG* 103 (Sept. 1981). DOI: 10.1115/1.3240816.

[5] P. W. Bearman and J. K. Harvey. "Golf Ball Aerodynamics". In: *Aeronautical Quarterly* 27.02 (1976), pp. 112–122.

[6] N. Beratlis, K. Squires, and E. Balaras. "AN EFFICIENT DRAG REDUCTION OF BLUFF BODIES BY TESSELLATION". English (US). In: Publisher Copyright: © 2022 12th International Symposium on Turbulence and Shear Flow Phenomena, TSFP 2022. All rights reserved.; 12th International Symposium on Turbulence and Shear Flow Phenomena, TSFP 2022 ; Conference date: 19-07-2022 Through 22-07-2022. 2022.

[7] Nikolaos Beratlis, Elias Balaras, and Kyle Squires. "On the origin of the drag force on dimpled spheres". In: *Journal of Fluid Mechanics* 879 (2019), pp. 147–167. DOI: 10.1017/jfm.2019.647.

[8] J. Choi, W. Jeon, and H. Choi. "Mechanism of drag reduction by dimples on a sphere." In: *Physics of Fluids* 18 (2006), pp. 149–167.

[9] Kwangmin Son et al. "Mechanism of drag reduction by a surface trip wire on a sphere". In: *Journal of Fluid Mechanics* 672 (2011), pp. 411–427. DOI: 10.1017/S0022112010006099.

[10] P. R. Spalart and J. H. Watmuff. "Experimental and numerical study of a turbulent boundary layer with pressure gradients". In: *Journal of Fluid Mechanics* 249 (1993), pp. 337–371.

[11] J. Yang and E. Balaras. "An embedded-boundary formulation for large-eddy simulation of turbulent flows interacting with moving boundaries". In: *Journal of Computational Physics* 215.1 (2006), pp. 12–40.